

3 **Automated Mapping of Clouds on Titan Using Semantic Segmentation**

4 ANONYMOUS AUTHOR(S)

5 **ABSTRACT**

6 Despite widespread adoption of deep learning models to address a variety of computer vision tasks,  
7 planetary science has yet to see extensive utilization of such tools to address its unique problems. On  
8 Titan, the largest moon of Saturn, tracking seasonal trends and weather patterns of clouds provides  
9 crucial insights into one of the most complex climates in the Solar System, yet much of the available  
10 image data is still analyzed manually. In this work, we apply a transfer learning algorithm to perform  
11 semantic segmentation of clouds in Titan images acquired by the Cassini spacecraft - a previously  
12 unexplored approach to a ‘big data’ problem in planetary science. We demonstrate that an automated  
13 technique can provide quantitative measures for clouds, such as areas and centroids, that may otherwise  
14 be prohibitively time-intensive to produce by human mapping. Furthermore, despite Titan-specific  
15 challenges, our approach yields accuracy comparable to contemporary cloud identification studies on  
16 Earth and other worlds. We compare the efficiencies of human-driven versus algorithmic approaches,  
17 showing that transfer learning provides speed-ups that may open new horizons for data investigation  
18 for Titan. Moreover, we suggest that such approaches have broad potential for application to similar  
19 problems in planetary science where they are currently under-utilized. Future planned missions to the  
20 planets and remote sensing initiatives for the Earth promise to provide a deluge of image data in the  
21 coming years that will benefit strongly from leveraging machine learning approaches to perform the  
22 analysis.

23 *Keywords:* Titan(2186) — Atmospheric clouds(2180) — Semantic segmentation — Transfer learning

24 **1. INTRODUCTION**

25 **1.1. Titan’s Meteorology**

26 Titan, Saturn’s largest moon, has an atmosphere  
27 denser than that of any other moon in the Solar System. It was revealed by the Cassini-Huygens mission  
28 to have a dynamic climate capable of supporting complex meteorological phenomena (Lorenz 1993; Griffith  
29 et al. 1998, 2000; Fulchignoni et al. 2005; Tomasko et al.  
30 2005; Griffith et al. 2009), including a ‘hydrocarbon cycle’ analogous to the water cycle on Earth. Titan’s atmosphere exhibits cloud formations (Griffith et al. 1998;  
31 Schaller et al. 2006a,b; Griffith et al. 2005), precipitation,  
32 and evaporation (Turtle et al. 2011; Barnes et al.  
33 2013; MacKenzie et al. 2014). In addition, the methane  
34 cycle apparently interacts with the surface through lacustrine reservoirs (Stofan et al. 2006) and fluvial erosion  
35 (Lorenz et al. 2008; Burr et al. 2013a,b) (see Figure 1).  
36 Understanding the seasonal weather patterns of these  
37 clouds is essential to developing a model for Titan’s atmosphere, which may also lend greater understanding  
38 into the atmospheric processes of other Solar System  
39 worlds including our own (Mitchell et al. 2011; Lora  
40 et al. 2015). However, obtaining a high-quality dataset  
41

42 of cloud locations, morphologies and other information  
43 comes with a host of challenges.

44 First, capturing high-quality images of clouds on Titan  
45 is not straightforward. The moon’s methane-rich  
46 atmosphere possesses a haze that is opaque to optical  
47 observations, excepting only specific ranges of the infrared spectrum (Turtle et al. 2011). Cassini’s Imaging  
48 Science Subsystem (ISS), one of two systems used to  
49 collect near-infrared images on the spacecraft, included  
50 several infrared filters capable of piercing the methane  
51 haze and enabling capture of cloud images (Porco et al.  
52 2004). While the cloud detection problem on Earth benefits  
53 from verification from multiple sources and spectral  
54 ranges, as utilized by Letu et al. (2022), Cassini’s  
55 ISS was only capable of using a single infrared filter  
56 at a time. Because the Saturnian year, and thus Titan’s as well, is 29.4 Earth-years long, Titan’s seasons last significantly longer than those on Earth (Rodriguez et al. 2009, 2011; Mouelic et al. 2018). For this reason, cloud development must ideally be observed over several Earth-decades to acquire a complete annual cycle. Consequently, the Cassini dataset built up over 127 Titan targeted flybys from 2004-2017 is the richest and most

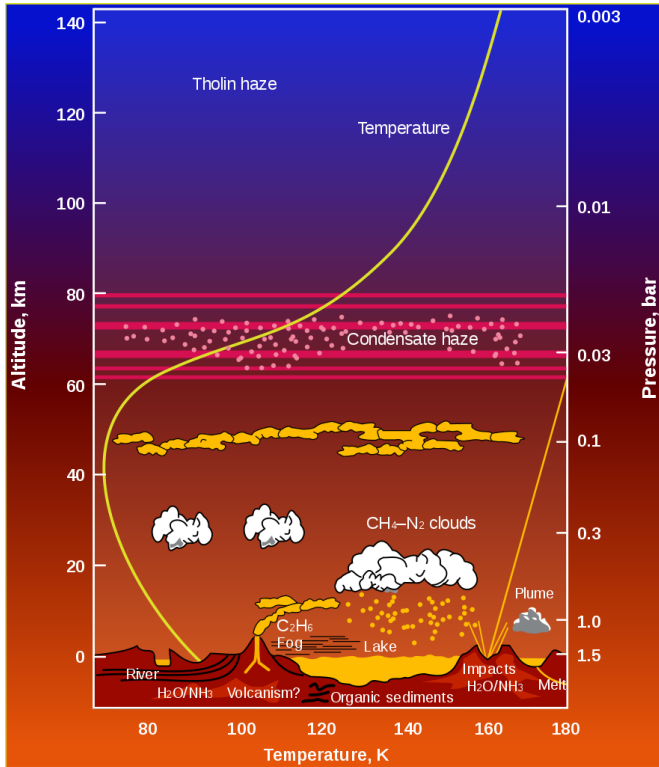


**Figure 1.** Schematic diagram of Titan's atmosphere, showing meteorological processes in the troposphere including the formation of methane-rich clouds at 15–30 km. Figure: NASA/JPL.

extensive collection of Titan images acquired to date. Specifically, while ground-based telescopes provide more temporal/spectral coverage, Cassini was capable of resolving individual clouds. Figure 2 shows examples of cloud-containing and cloud-free images acquired by the Cassini ISS with the CLR-CB3 filter, which has an effective wavelength of 938 nm.

Planetary scientists have labored to manually comb through the Cassini image data to establish basic trends and features of the clouds (Turtle et al. 2018), but there is still much to uncover. Experts in the field are interested in tracking cloud areas, shapes, locations and local times over multi-year periods. While this kind of specific information is fairly onerous for manual tabulation over the entire mission, and thus its collection has never been attempted, a rapid, automated method of deriving cloud parameters would provide a critical resource that may be used to improve the accuracy of atmospheric models of Titan (Brown et al. 2010).

### 1.2. Machine Learning Approaches Already in Use for Planetary Atmospheres

Recent advances in remote sensing research of the Earth's atmosphere can provide insights into how au-

tomated cloud detection might be approached on other worlds. The vast majority of cloud identification research focuses on terrestrial applications due to the immediate relevance to human society and multitudinous high-quality data sources. Before the popularization of deep learning, classic approaches such as handcrafted feature representations saw moderate success. While capable in some cases, these models struggled to generalize to the diversity of Earth weather, a substantial drawback given the wide variety of cloud formations possible on Earth (Mahajan & Fataniya 2020; Li et al. 2021). Deep computer vision models, including fully convolutional networks, have proven to be more effective in side-by-side comparisons (Goff et al. 2017). Several specialized approaches have been implemented, including multi-scale convolutional feature models that incorporate multiple layers of the same image from different sensors (e.g. RGB and infrared) (Li et al. 2019), ensemble approaches with independent feature extraction and boundary refinement modules (Chen et al. 2021), and many others. Semantic segmentation architectures are also popular, especially the U-Net (Francis et al. 2019) and ResNet (Mommer 2020) architectures. Semantic segmentation involves producing a mask that labels the individual pixels of an image. These techniques have demonstrated per-pixel accuracies as high as 0.9 for terrestrial cloud applications (Francis et al. 2019; Li et al. 2021; Goff et al. 2017; Mommer 2020). Some deep learning approaches have even become advanced enough to target specific cloud formations. Developed a U-Net model for detecting Above Anvil Cirrus Plume (AACP) formations, a reliable predictor of imminent severe weather. Other approaches demonstrate the feasibility of cross-scene hyperspectral classification (Zhang et al. 2021b,a, 2022). These significant advances in cloud detection are possible because of the vast quantities of image data available through several satellites orbiting the Earth, enabling the full capabilities of deep learning.

Deep learning has revolutionized computer vision by using very large networks with dozens of layers to model rich relationships between individual features (LeCun et al. 2015). At the present day, the most widely known and utilized are Convolutional Neural Networks (CNNs), particularly in application to image classification and object detection tasks (Krizhevsky et al. 2012). However, designing and coding a new deep learning model is difficult, time consuming, data-intensive, and therefore often beyond the scope of a typical project's time and resource budgets. Popular architectures often involve hundreds of millions of parameters, resulting in massive computational costs for even the simplest training.

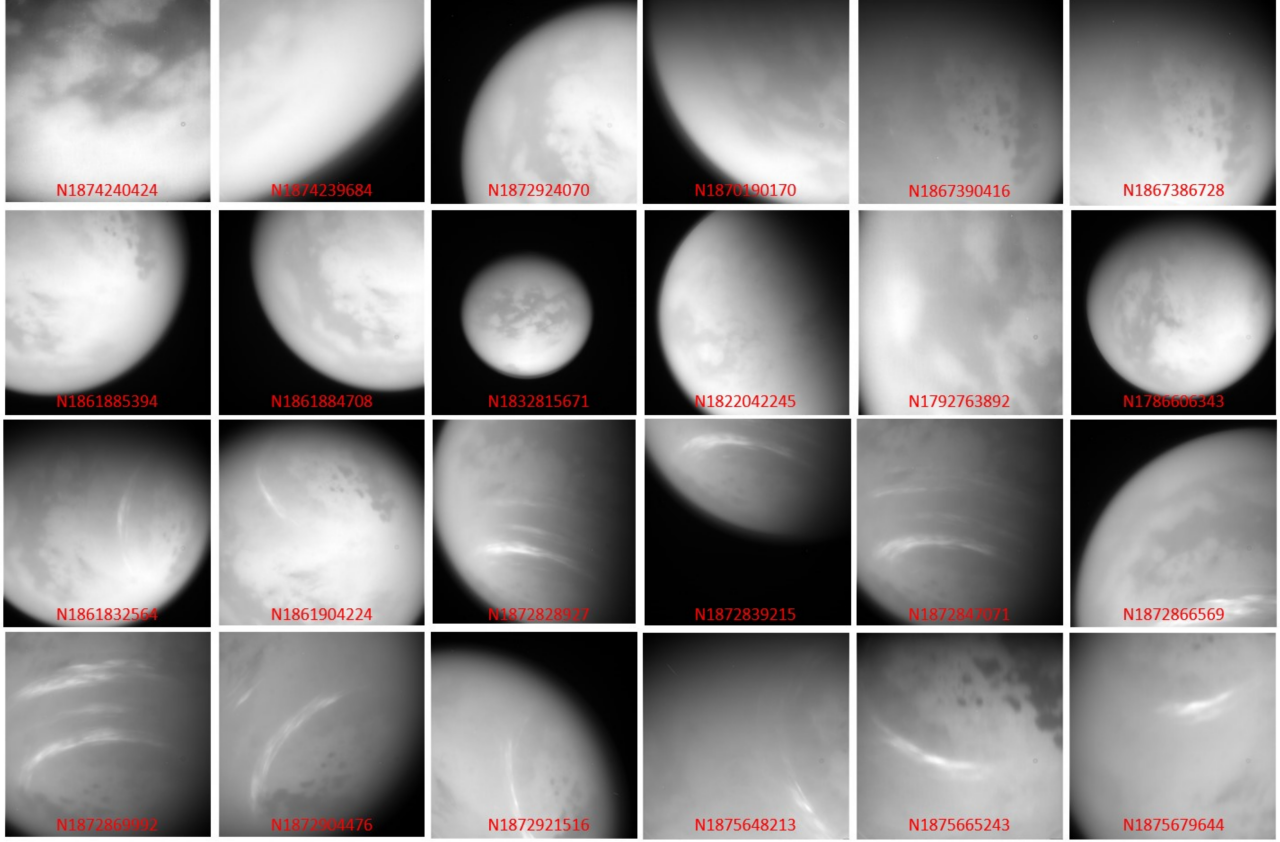


**Figure 2.** Examples of images in the Cassini ISS dataset taken with the Narrow Angle Camera (NAC) CLR-CB3 filter: upper two rows - no clouds. Lower two rows - with clouds. Image names as listed in NASA planetary data system (PDS) provided (NASA/JPL/SSI).

145 By taking advantage of similarities between domains,  
 146 transfer learning addresses problems with limited data.  
 147 Transfer learning leverages increasingly complex learned  
 148 features at progressively deep layers in a neural network,  
 149 based on the premise that the foundation of learned  
 150 features from one domain are still broadly applicable  
 151 to tasks in other domains. Because many of the best  
 152 pretrained models target a broad array of classes via  
 153 datasets like **ImageNet**, their early layers are applicable  
 154 to a wide range of computer vision problems. Transfer  
 155 learning takes advantage of this to preserve early learned  
 156 features by ‘freezing’ those layers and only training the  
 157 last few layers of a network on a novel dataset. Typi-  
 158 cally, very large models are trained on datasets with  
 159 many classes and examples, enhancing their broad fea-  
 160 ture detection capabilities. This is advantageous for  
 161 transfer learning applications, as it allows for the utili-  
 162 zation of large, well-trained models with pre-trained  
 163 weights to be tuned on a only small amount of new  
 164 data with a few additional training epochs and orders  
 165 of magnitude fewer training examples. In summary,  
 166 transfer learning reduces the dependency on large train-  
 167 ing datasets and dramatically cuts down on training

168 time (Zhuang et al. 2020). Transfer learning has been  
 169 shown to be especially efficacious in computer vision  
 170 problems (Li et al. 2020). Example use cases include  
 171 forestry (Kentsch et al. 2020), pavement fault detec-  
 172 tion (Gopalakrishnana et al. 2017), and facial recogni-  
 173 tion (Cao et al. 2013). For these reasons, we explored  
 174 transfer learning as an efficient way to train models for  
 175 Titan cloud identification.

### 176 1.3. Application to Titan

177 Image-based Titan cloud identification is especially  
 178 challenging due to the high variability of cloud shapes,  
 179 sizes, opacity, latitudes, and the lack of contrast with  
 180 the surface of Titan. These difficulties are illustrated  
 181 in the example images in Fig. 3. Other planets present  
 182 similar difficulties and opportunities. With the excep-  
 183 tion of Mercury, every planet in the Solar System has  
 184 a dynamic atmosphere that results in cloud formations.  
 185 Each has a distinct surface colorization, texture, and  
 186 exhibits other conditions that make it unique. Designing  
 187 individual machine learning models for each world,  
 188 many of which have very limited data available, is infea-  
 189 sible. While some previous publications mention com-

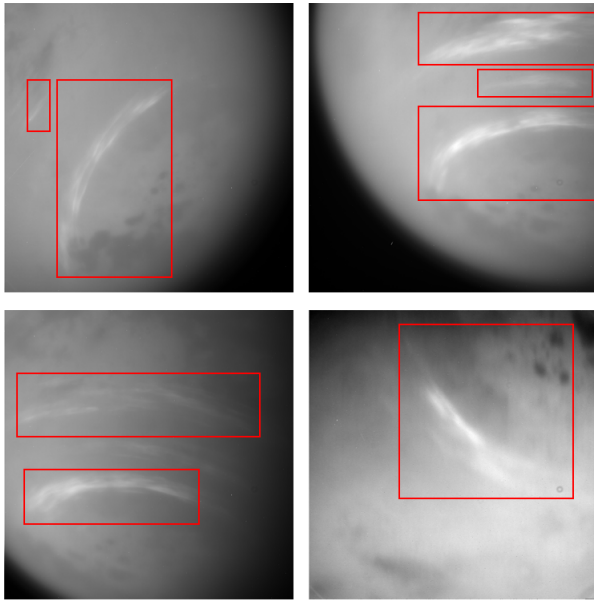


**Figure 3.** Examples of variability in Titan cloud formations from Cassini data. Cloudy regions are bounded in red for emphasis. Images left to right, top to bottom: N1872904476, N1872867349, N1872850511, N1875653333

puterized cloud detection (e.g. Turtle et al. (2018)), the only dedicated example in the literature involves using a Bayesian Source Separation algorithm paired with Markov Chain and Monte Carlo simulation methods (et al. 2010; Mouelic et al. 2018). Therefore, there is considerable scope for further application of machine learning to planetary cloud detection and other science areas, given the veritable explosion in development of new deep learning techniques in the last decade.

#### 1.4. Contribution and Significance

Although machine learning has been utilized for other NASA purposes such as spectroscopy (Wilkins et al. 2020), mars rover vision systems (Dundar et al. 2019), crater detection (Di et al. 2014), and more, its adoption in the planetary science community has been slower, perhaps due to historically smaller datasets than in other areas. In a white paper for the *NRC Planetary Science and Astrobiology Decadal Survey*, 51 researchers signed a statement emphasizing a pressing need for machine learning to be more widely deployed in planetary science projects. They note that the proportion of planetary science papers that include machine learning is less than half of that in the other three NASA science areas: heliophysics, astrophysics, and Earth science (Azari et al. 2020).

In this paper, we exploit and demonstrate how a deep learning computer vision approach can deliver accurate and efficient models for Titan cloud identification based

a subset of the available data. To our knowledge, this work is the first to implement a deep learning computer vision model for the purpose of Titan cloud feature recognition. We implement a semantic segmentation model to identify whether or not a Cassini image of Titan contains one or more cloud formations, and which image pixels are contained within the cloud. This discrimination is essential for determining the spatial distribution of clouds over an extended time period, which is a topic of considerable interest for researches into Titan meteorology (Turtle et al. 2018; et al. 2010). We then use the masks generated by our semantic segmentation model to calculate the areas, centroids, and aspect ratios of Titan clouds, providing valuable metrics that were previously too labor-intensive to be calculated by hand. Furthermore, we show that this approach is faster than manual tabulation, and consistent with contemporary applications to other contexts. In addition to developing a model that effectively identifies clouds on Titan from historic Cassini data, we envision that future data pipelines may be implemented onboard spacecraft to process real-time data from missions to Titan and other planets. The ability to create higher-level data products on board spacecraft would in turn enable substantial reduction in data downlink requirements.

## 2. MATERIALS AND METHODS

In this section we present a novel cloud identification model for addressing the challenges outlined in Section 1 by classifying images with a convolutional neural network (CNN) based on ResNet50, a popular image classification architecture (Simonyan & Zisserman 2015). We provide an overview of this strategy, an image preprocessing approach, and our transfer learning implementation.

### 2.1. Data Set

Cassini ISS image data is publicly available via NASA's Solar System Image Archive hosted at the Jet Propulsion Laboratory (JPL) and also via NASA's Planetary Data System (PDS). Despite providing clear views of an extensive variety of cloud morphologies, the Cassini images are monochromatic, as evident in Figure 3. While Cassini's ISS does benefit from having multiple filters, it may only use two at a time for each of the Narrow Angle Camera (NAC) and the Wide Angle Camera (WAC). Therefore, the large number of filters designed to target specific spectral bands poses an initial question in terms of which filters are the most optimal to use for cloud detection. Moreover, Cassini's position with respect to Titan varied significantly throughout the course of the mission. While Earth-based satellites typically orbit at a constant planeto-centric distance, giving images

269 a consistent pixel scale, Cassini followed an orbit around  
 270 Saturn that brought it from less than 5,000 km to great  
 271 than 5 Mkm from Titan during the mission. Thus, its  
 272 images were captured from diverse viewing angles with  
 273 disparate lighting conditions and resolutions. We sum-  
 274 marize the challenges with the Cassini image dataset as  
 275 follows:

- 276 1. Cloud shape and size variability, ranging from nar-  
     row streaks to pseudo-elliptical masses;
- 277 2. Serial, monochromatic image data, meaning that  
     data from different filters are separated in time  
     and viewing angle and therefore cannot be treated  
     as multiple color planes of the same image;
- 278 3. Image artifacts and noise, an issue in common with  
     other image data;
- 279 4. Lack of cloud-surface contrast, especially towards  
     high surface viewing angles (planetary limb);
- 280 5. Cassini’s varying distance to Titan, creating a non-  
     uniform pixel scale in the images.

288 In this work, we started with all Titan data captured  
 289 by Cassini’s Imaging Science Subsystem (ISS) NAC from  
 290 June 2004 to October 2017, the full length of the Titan  
 291 viewing window. In order to narrow this dataset to a  
 292 more homogeneous and high-value set, we considered  
 293 only the 14,355 images from the ISS NAC’s CB3 in-  
 294 frared filter. This filter operated at 938 nm, which was  
 295 ideal for piercing the thick organic haze of Titan’s at-  
 296 mosphere. At this wavelength, clouds were clearly dis-  
 297 cernible as high-albedo shapes against the less reflec-  
 298 tive surface of Titan, though their visibility still varied  
 299 widely depending on factors such as proximity to the  
 300 planetary limb. We restricted our images to the NAC’s  
 301 CB3 filter because it provided a sufficient amount of  
 302 high-quality images for our purposes. Future work may  
 303 explore extending our methods to other filters that are  
 304 also capable of piercing Titan’s atmosphere. Each im-  
 305 age is either  $1024 \times 1024$  or  $512 \times 512$  pixels with a single  
 306 8-bit grayscale amplitude. All images were resized to  
 307  $512 \times 512$  for consistency. We provide our full dataset  
 308 online as described in Data Availability below.

309 Prior work has also shown that clouds were not dis-  
 310 persed evenly throughout the mission time window, but  
 311 rather appeared in high densities during specific months  
 312 ([Turtle et al. 2011](#)). We selected a window of November  
 313 2015 to September 2017 in order to capture one of these  
 314 high-density periods. From this window we selected 798  
 315 total images. We further separated these 798 images into  
 316 training and validation sets: 429 for training, and 369

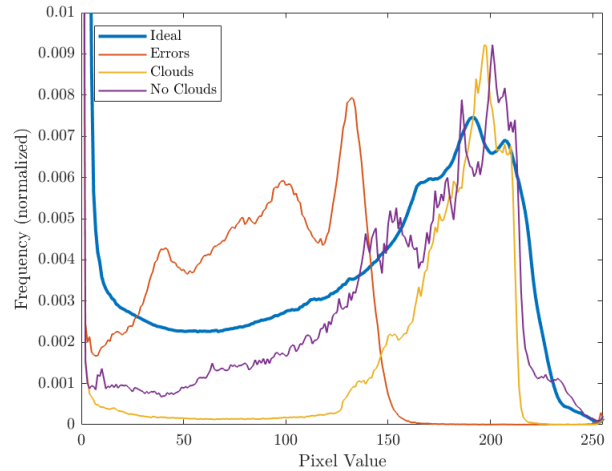


**Figure 4.** Brightness histogram comparison. In blue, the normalized histogram of the entire training set. In red: an image with artifacts and distortions. In orange: a high-quality image with clouds. In purple: a high-quality image without clouds. Note that the y-axis is normalized so that the area of the histogram sums to one, and that the y-axis is limited because black is by far the most dominant shade in images of Titan. Black pixels are located either on the dark side of Titan (not illuminated) or are on the sky.

317 for validation. These images are a representative sample  
 318 of the wide variety of cloud types and image conditions  
 319 in the Cassini data. All images that were used for train-  
 320 ing were labeled by hand using LabelMe. Labels were  
 321 bounding polynomials where every pixel enclosed in the  
 322 polynomial is considered part of the cloud. Multiple in-  
 323 stances of clouds each had distinct labels within a single  
 324 image.

325 Note that starting from  $\sim 15,000$  images and ending  
 326 with a set of around  $\sim 800$  is symptomatic of the quality  
 327 of images taken by Cassini, and also their redundancy.  
 328 Often, dozens of images will show the same cloud for-  
 329 mation, diminishing their usefulness for model training.  
 330 Rather than use as many images as possible, we focused  
 331 instead on a high-quality sample that reflects an expert  
 332 curated view of Titan clouds for our first analysis. Do-  
 333 ing so also demonstrates the efficacy of transfer learn-  
 334 ing for problems with smaller datasets, given that many  
 335 other Solar System worlds do not benefit from as plen-  
 336 titiful datasets as Cassini’s of Titan.

## 337 2.2. Data Cleaning

338 Planetary science exhibits many unique data collec-  
 339 tion challenges that distinguish it from other domains.  
 340 Many images from Cassini are unusable for analysis of  
 341 Titan’s weather phenomena, either because they con-  
 342 tain obtrusive artifacts, have too low a spatial resolu-  
 343 tion (captured from too far away), or they otherwise

contain too little of the moon. Such images are common on robotic planetary exploration missions, so pre-processing to constrain image quality is crucial. Including poor quality images in a training dataset makes the classification problem more complicated; instead, we simplify the task by automatically pre-screening and removing these undesirable images before they reach the model, as described below. In future works, this pre-processing might be fine-tuned using additional conventional computer vision techniques. We expect this to be an important part of implementing deep learning models for upcoming missions, and this may be a subject of future research.

Spectral analysis of pixel brightness shows potential for an efficient first pass to remove blatantly unusable images. To that end we computed brightness histograms, a frequency plot for each grayscale pixel value from 0 to 255, summarizing the image content, and enabling rapid identification of unsuitable images. Such images tend to have large, dark artifacts, or Titan is too small in the frame to permit a cloud search. In either of these cases, the brightness histograms skewed towards darker pixel values, differentiating it from the typical image. We used these histograms to automatically remove aforementioned erroneous images from the Cassini dataset. In order to determine which images contained prohibitive errors and which were usable, we compared the histogram of each image with an ‘ideal’ histogram that was composed of images without errors. We established this ideal histogram by computing a normalized histogram for the sum of all images in the training dataset, as shown in Fig. 4. The cosine similarity of two histogram vectors A and B is given by:

$$\text{sim}(A, B) = \frac{A \cdot B}{\|A\| * \|B\|} \quad (1)$$

To automatically filter out the undesirable images, we employed a threshold of  $\text{sim}(A, B) < t$ . In our testing, we found that a threshold value of  $t=0.95$  tended to preclude most of the undesirable images, though this could be tuned based on the given problem. We selected this threshold because it empirically demonstrated sufficient filtering to preclude undesirable images.

Note that the brightness histograms alone are not enough to distinguish whether or not an image has clouds, as the curves are too similar. It is only suitable as a means of identifying unusable images. Due to high variability of cloud formations, complexities involving the angle of the sun, and non-uniform capture time, it is evident that a naive signal processing approach will not provide adequate selection nor filtering capabilities, and is only sufficient to sort out images that will not

provide any useful information. Rather than relying on global metrics, an effective classifier must exploit local structure to be useful.

### 2.3. Model Architecture and Training

Our ResNet50 CNN (architecture in Figure 5) was pre-trained on the Common Objects in Content (COCO) dataset (Lin et al. 2014) to learn general feature detection for a wide variety of objects (He et al. 2015). COCO contains over 14 million images relating to tens of thousands of classes. Per a transfer learning approach, we then tuned this pre-trained version to our specific use case, applying our own training using the pre-selected and labeled subset of Cassini images. We trained with a binary cross-entropy loss function, which converged after 20 epochs.

### 2.4. Metric Calculation

Given a segmented mask output for each input image, our goal was to build a framework for calculating metrics such as cloud area, centroid coordinates, and aspect ratio, with the potential for additional metrics in the future based on input from other researchers. We made use of data from NASA’s (JPL) Planetary Data System (PDS) and code published in Seignovert et al. (2017, 2021) to obtain back planes for latitude, longitude, declination, and right ascension for each pixel in each image (Acton 1996; Acton et al. 2017). This data is specific to each image, meaning it accounts for the varying angle and distance of Cassini with respect to Titan throughout the mission. This data was only collected for the 369 images used in the validation set. Given this data, we then superimposed a grid onto the mask. Because this grid was placed on a spherical surface, the curvature of Titan and viewing geometry means that the grid cell areas decreased as they progressed towards the poles.

Grid cells were generated such that they were equally spaced in latitude and longitude. Any two cells at the same latitude (for example, all cells that border the equator) shared identical areas. To account for the decrease in area as the cells approached the poles, we calculated a unique area for the cells in each latitude circle equal to the cosine of the latitude of the center of that band times the area of a cell at the equator. Given a known area for each cell in the grid, we can then calculate our metrics of interest. The number of cells in the grid can be configured to decrease the generation time at the expense of measurement accuracy. Grids of varying precision are shown in Figure 6.

Total feature area is the sum of the areas of all cells that have some overlap with the segmented mask. For portions of the cloud that only partially overlap with a

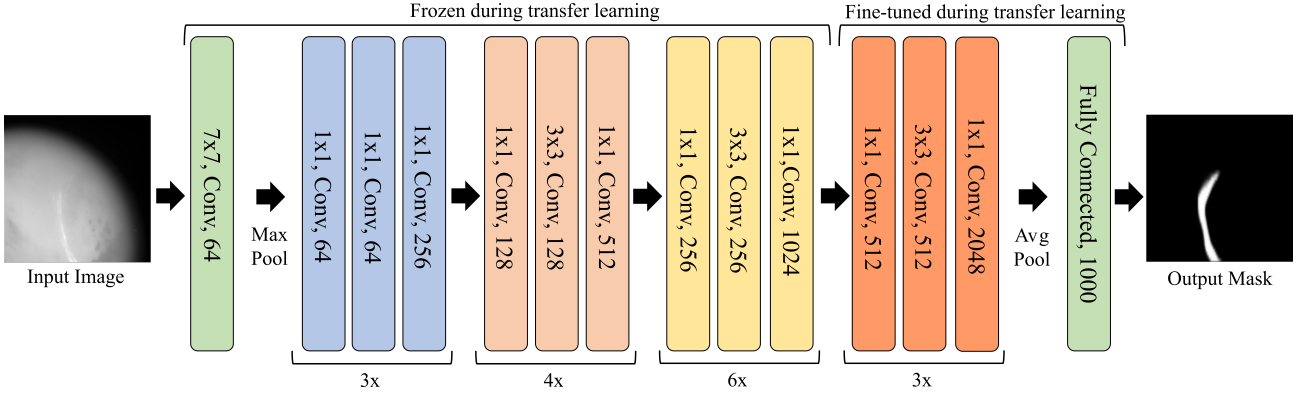


**Figure 5.** Architecture of a standard ResNet50 model. Image data are fed in from the left to the initial convolution layer, processed by subsequent layers, and then produce a mask of the same dimensions as the input.

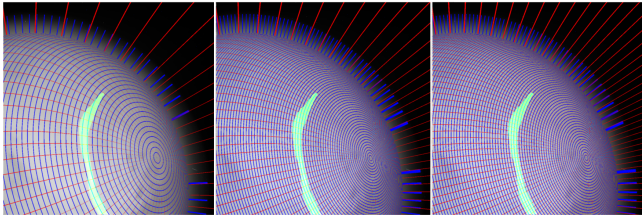


**Figure 6.** Three examples of varying grid sizes superimposed onto model-labeled mask. From left to right: 90×60 cells, 120×90 cells, 150×120 cells. Image: N1872921516

cell, this proportional area was approximated by counting the number of pixels that overlap and dividing it by the total pixels in the cell, then treating that as the proportion of the total cell area.

The centroid was calculated as a weighted center of mass, treating the center of each cell as a point with a single latitude and longitude, multiplied (weighted) by the percentage overlap of that cell with the segmented mask. The weighted longitude and latitude of each cell was multiplied by that cell's area and summed across all cells. That total was then divided by the cloud total area to find the weighted average longitude and latitude of the cloud overall.

Finally, we define the aspect ratio of the cloud as the ratio of its latitudinal extension to its longitudinal extension. We calculated this by finding the greatest distance between any two points at the same latitude, divided by the greatest distance between any two points at the same longitude. Note that the grid was designed such that the user can decide on the resolution of cells to use, at the expense of possibly slower run-times for larger numbers of cells. Using these grids, it is also possible to generate additional metrics beyond the ones that we produced. For example, other researchers may be interested in the slope of the line of best fit applied to the cloud, or a cloud's curvature. A full tabulation of metric calculation results is provided as supplementary material.

### 3. RESULTS

In this section we present our results from using the methodology described above to train the model, and then applying the trained model to our testing dataset. We accomplished this by feeding the segmented masks of the testing set into the gridding software to calculate metrics for a subset of the Cassini data.

#### 3.1. Segmentation

We first evaluate model performance on the basis of how well it identified individual instances of clouds, not on a per-pixel level. To quantify this, we make use of accuracy, precision, and recall. Accuracy reflects how many total guesses, positive and negative, are correct. Precision denotes how often a positive guess is correct. Recall indicates, given that a cloud exists in an image, how likely the model is to detect and correctly classify it. These are all calculated as follows (TP is true positive, TN is true negative, FP is false positive, FN is false negative):

$$\text{Accuracy} = \frac{TP + TN}{Total} \quad (2)$$

$$\text{Precision} = \frac{TP}{TP + FP} \quad (3)$$

$$\text{Recall} = \frac{TP}{TP + FN} \quad (4)$$

On the 369 images in the test set, the model achieved an accuracy of 0.83, a precision of 0.95, and a recall of 0.75.

We then evaluate how well the model classified pixels in a given image, contributing to the overall efficacy of the segmented mask output. We make use of the intersection over union (IoU) score, which is calculated as follows:

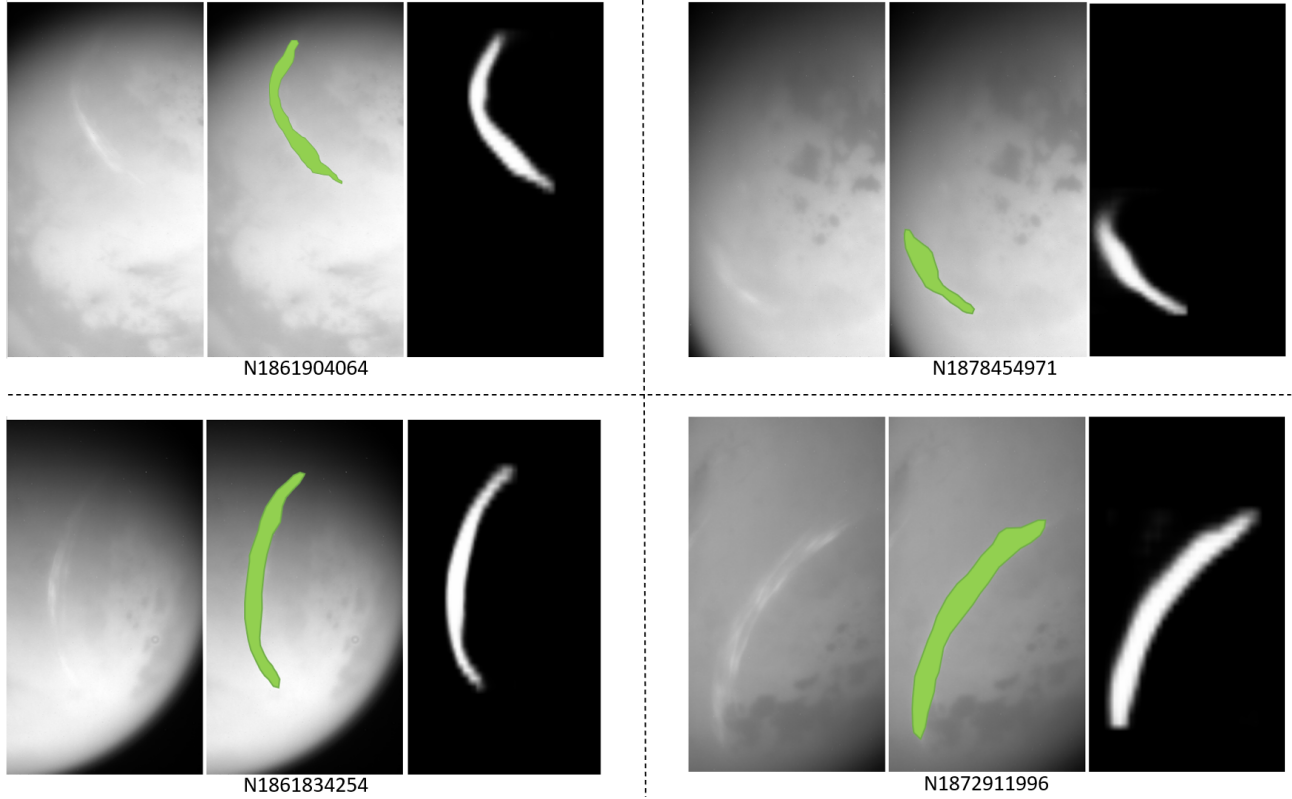


**Figure 7.** Instances where the model struggled to find precise edges of the clouds. Left is original image, center is human ground-truth label, right is mask produced by the model.

$$\text{IoU} = \frac{\text{TrueMask} \cap \text{GuessedMask}}{\text{TrueMask} \cup \text{GuessedMask}} \quad (5)$$

Thus the minimum IoU score is 0, when the output mask shares no overlap with the true mask (or the model guesses that there is no cloud in the image when in fact there is), and the maximum is a score of 1, when the output mask and true mask are completely aligned. This IoU score was calculated for each image and then averaged across all images to obtain a mean IoU of 0.77 for the testing set. The testing set contained examples of images that did not contain clouds, however, the IoU was only calculated for images where the model predicted the presence of at least one cloud. If an image contained a cloud that the model did not identify, then it received an IoU score of 0 for that image. In many cases, the model correctly identified the general location of the cloud formations in an image, but struggled to precisely outline the edge of the cloud structure. Even for a human, identifying where these edges stop and the atmospheric haze begins is challenging. This struggle with edge detection likely contributed to a lower IoU score. Examples of these cases are shown in Figure 7.

### 3.2. Grid Calculation of Cloud Metrics

We also generated a series of graphs to illustrate how the grid approaches can visualize trends in clouds over the course of the Cassini mission, such as a histogram showing the distribution of cloud areas or aspect ratios. All graphs were generated using a grid of  $90 \times 80$  cells. Figure 8 shows two plotted examples. These plots show that the clouds tend to cluster in a size range between  $300,000 \text{ km}^2$  and  $500,000 \text{ km}^2$ , and extending to greater size in longitude than in latitude. This reflects established trends in Titan clouds during the window when Cassini captured our dataset. [Turtle et al. \(2018\)](#)

Our approach can also produce graphs that reflect trends over a time period, such as how cloud centroids might shift in latitude or cloud areas might grow with the seasons. Figure 9 provides examples of these graphs. These also reflect trends that are supported by existing observations. During 2017, aspect ratios tended to stay constant, shifting slightly towards a decrease in latitude and an increase in longitude. Likewise, centroid latitudes remain relatively constant around  $\sim 60^\circ$  throughout that time period, as seen in previous studies. [Turtle et al. \(2018\)](#)

Note that these figures are intended as examples; complete analysis of the trends would require applying our approach to a larger sample size of the Cassini data. Our

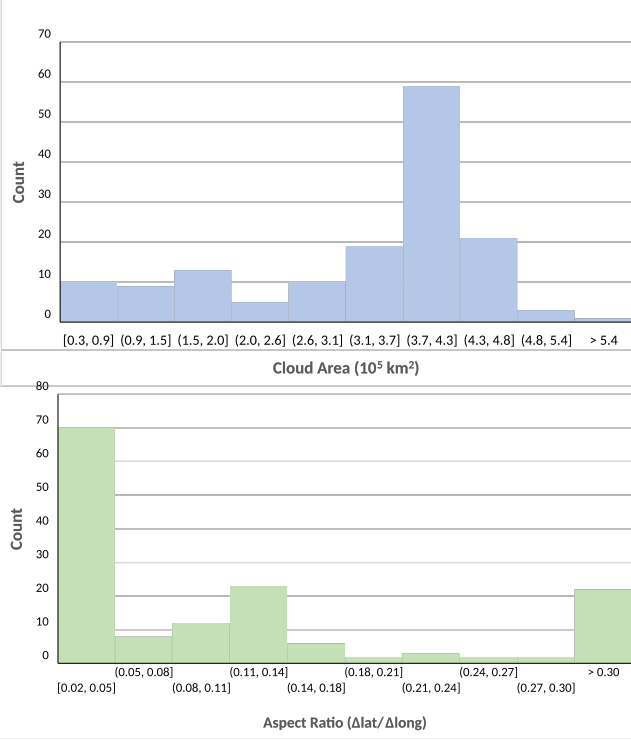


**Figure 8.** a) Cloud areas histogram for the test data. b): Cloud aspect ratio histogram for the test data.

goal is to demonstrate an efficient and accurate tool for producing such metrics, so that other Titan researchers can adopt such approaches in future work.

### 546 3.3. Speed Comparison of Machine Learning versus 547 Manual Approach

548 To understand the speed at which our methods can  
549 compute information of interest, we recorded how much  
550 time was required on average to perform inference on  
551 an image and then extract said metrics. Averaged over  
552 all 369 images of our testing set, computing the seg-  
553 mented mask for a  $512 \times 512$  image required 10 seconds  
554 on a Google Cloud t7 GPU. Based on the time required  
555 to label the training data, we estimated that drawing a  
556 label of similar quality would take at least 30 seconds  
557 for a trained human, potentially longer for more com-  
558 plicated cloud geometries. For images that contain an  
559 instance of clouds, computing area, centroid, and aspect  
560 ratio required an average of 75 seconds with a  $90 \times 80$   
561 grid on an Intel i7 CPU. To our knowledge, nobody has  
562 attempted to manually compute these metrics, so it is  
563 difficult to compare this with human rates.

564 At these speeds, generating labels for all 14,335 images  
565 provided by the CB3 filter would take approximately 40  
566 hours. Generating metrics for these images would take  
567 an additional 300 hours in the worst case. Although it  
568 is difficult to compare this to human performance, the

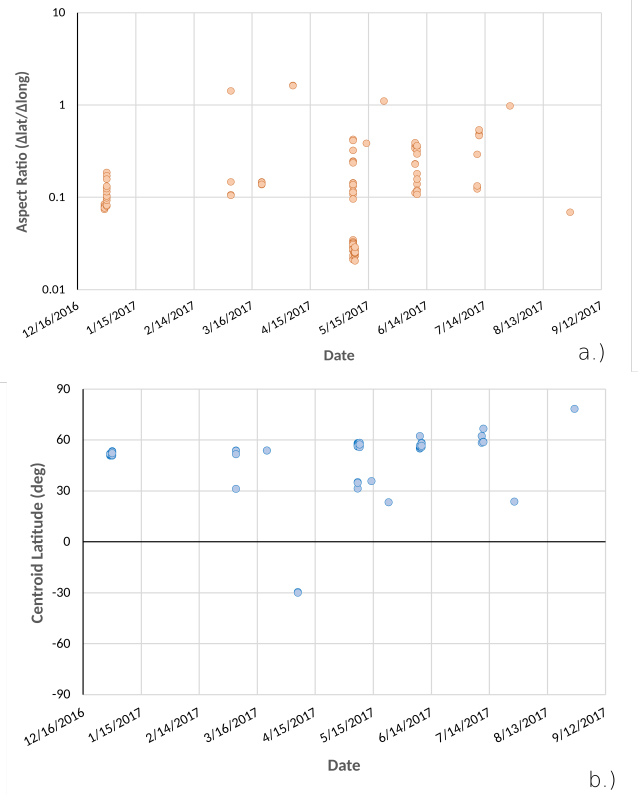


**Figure 9.** a) Cloud aspect ratio over time. b) Centroid latitude over time. Note that clouds are condensed into vertical columns because images could only be captured during discrete flyby time windows.

569 obvious advantages of running this processing 24 hours  
570 a day without supervision improves upon human efforts.  
571 Furthermore, there is potential for significant speedups  
572 by applying multi-threading, parallelization, and faster  
573 hardware. It is also worth noting that this comparison  
574 would change if the model were deployed on-board a  
575 spacecraft, since radiation-hardened computers do not  
576 possess the same processing power as modern GPUs.

## 577 4. DISCUSSION

578 Our results indicate that automated cloud identifi-  
579 cation on images of Titan from the Cassini mission is  
580 tractable, and that semantic segmentation is an effec-  
581 tive approach. We have shown that during training, the  
582 model converges rapidly and demonstrates a high val-  
583 idation accuracy of 0.83 with a precision of 0.95. We  
584 note that our accuracy, recall, precision, and IoU scores  
585 are comparable to similar cloud identification and seg-  
586 mentation works on Earth. Goff et al. (2017) used a  
587 convolutional neural network for this purpose, achiev-  
588 ing a precision score of 0.81 and a recall of 0.75. Simi-  
589 larly, Li et al. (2021) fused high-resolution satellite data  
590 from multiple sensors to achieve an average IoU of 0.9

and an accuracy of over 0.95. Francis et al. (2019) also demonstrated the efficacy of U-Net, another popular semantic segmentation architecture, recording a 0.91 accuracy. Lopez-Puigdollers et al. (2021) take advantage of pre-labeled datasets for Landsat-8 and Sentinel-2 to achieve an accuracy of 0.94 with a fully-connected approach. Our work on Titan demonstrates similarly high scores despite the difference in image quantity and quality compared to terrestrial remote sensing.

Numerous planetary science projects may also benefit from this technology. Caille et al. (2022) already demonstrate that k-means clustering is effective for clouds on Mars, noting that their approach might be further improved by deep learning. Similarly, Machado et al. (2022) highlight their intention to apply deep computer vision to their cloud tracking efforts on Venus. Image datasets for cloudy worlds including Jupiter, Uranus, and Neptune are all also available in NASA’s Planetary Data System, and have seen few, if any, deep learning projects Chanover et al. (2022). The effectiveness of our approach, with limited data and computational resources, should give encouragement to future researchers who face similar limitations that fundamental and important scientific information can be readily extracted.

In contrast to manual approaches, machine learning techniques have the potential to enable precise tracking of clouds across many years of images, processing large image quantities significantly faster than any human. Thus, such techniques can save planetary scientists countless hours by automating scientific tasks such as cloud tabulation and mensuration. They also stand to further the state of the art by enabling the recognition of subtle trends and patterns that have never before been discernible, but emerge only after systematic quantitative analysis. Such techniques can be used to rapidly compute cloud areas, centroids, aspect ratios, and other useful metrics, allowing researchers to reevaluate existing datasets and to attempt to answer otherwise prohibitively labor-intense problems. Having detailed cloud shape outlines may permit comparison with regional, mesoscale cloud models such as TRAMS (Barth & Rafkin 2007, 2010; Rafkin & Barth 2015; Rafkin & Soto 2020; Rafkin et al. 2022) We also expect that researchers will apply their own domain knowledge to labelling such datasets for use in training deep learning models, enabling their deployment for other specific problems.

In addition to processing data after missions are complete, these models may be beneficial for in-flight data reduction as well. One of the most significant problems facing robotic missions is downlink bandwidth: only limited quantities of information can be transmitted back

to Earth, especially for more distant missions using the Deep Space Network (DSN). As spacecraft cameras become more advanced, with larger detector arrays and increased dynamic ranges in sampling, increasingly large image files must be compressed and transmitted. Without a means of identifying useful images, a mission is currently compelled to either store and eventually transmit all of them over a long time period (as with New Horizons), or else to transmit only a subset of the data. This bandwidth bottleneck currently affects missions to every world in the Solar System, including major future missions such as Europa Clipper (Phillips & Pappalardo 2014). Similarly, the upcoming DAVINCI mission to Venus will already deploy a Generative Adversarial Network (GAN) for its Compact Ultraviolet Imaging Spectrometer (CUVIS) that will “generate a reduced data set...and help flag and prioritize full-resolution data” (Garvin et al. 2022). This demonstrates how some missions might also use on-board image segmentation models to determine which images are valuable and which to discard before transmitting. Our work provides a step towards addressing these unique opportunities and challenges in various planetary science contexts, including imaging of Titan. Decreasing transmission volume and processing speed becomes increasingly relevant given the anticipated influx of Titan image data due to several key endeavors in the coming decade (e.g. Dragonfly (Barnes et al. 2021)). Although our model may not yet be suitable for implementation on a spacecraft (depending on available computing power), it demonstrates that this is likely to be a feasible approach in the future.

Besides data processing for close-up space missions, extracting cloud feature parameters from more distant telescopic observations may also be possible. The recently-launched James Webb Space Telescope (JWST) possesses an angular resolution as high as 0.”04 (with NIRCam), which is capable of capturing images of Titan at modest spatial resolution ( $\sim$ 220 km/pixel). Several ground-based telescope projects are also in development that will offer higher resolutions, including the European Space Agency’s Extremely Large Telescope (EELT), which is anticipated to be commissioned in  $\sim$ 2027, the 25 m GMT (Giant Magellan Telescope) in Chile, and possibly also the Thirty Meter Telescope (TMT) which is currently searching for a site. With 25–39 m apertures and adaptive optics, these observatories will possess a resolving power capable of capturing medium resolution images of Titan, up to  $200 \times 200$  pixels. This will significantly increase the availability of resolved cloud data of Titan and other worlds.

Additionally, our work is intended to promote a reevaluation of existing expectations of the difficulty and time

695 commitment to utilize machine learning tools in planetary science research. Though our work addresses only  
 696 the sole problem of cloud identification, there are many other image analysis problems that may be suitable for  
 697 application of transfer learning methods, as well as more sophisticated image processing techniques. In particular we suggest that wider application to surface features identification as well as atmospheric discrimination may prove to be not only tractable, but also yield novel results.  
 704

## 705 5. CONCLUSION

706 In this paper we presented a novel approach to Titan  
 707 cloud identification using transfer learning to effectively label the individual pixels of images of Titan. Despite  
 708 Titan-specific challenges, our results are comparable to similar studies on Earth despite disadvantages  
 709 in data availability and quality. We extracted key metrics including cloud areas and centroids that may be  
 710  
 711

713 prohibitively time consuming to compute manually, and  
 714 analyzed the efficiency of our technique. We demonstrated how our approach can elucidate trends in cloud  
 715 development over the course of the Cassini mission.  
 716

717 Given upcoming missions to Titan and advances in  
 718 ground-based telescopes, there is a need for robust,  
 719 proven models that can process high-quality and large-  
 720 quantity data. Even now, six years after the mission  
 721 concluded, there is much to be learned from novel pro-  
 722 cessing of Cassini data at scale. We show that deep  
 723 learning techniques can be significantly more efficient  
 724 than manual tabulation, especially given increasingly  
 725 large datasets as spacecraft technology improves. We  
 726 hope that this work motivates other planetary science re-  
 727 searchers to implement deep models with transfer learn-  
 728 ing for other problems in planetary science, so that the  
 729 field as a whole might enjoy the benefits of transfer learn-  
 730 ing for computer vision.

(Acknowledgements anonymized for review)

## REFERENCES

- 735 Acton, C. 1996, Planetary and Space Science, 44, 65,  
 736 doi: [10.1016/0032-0633\(95\)00107-7](https://doi.org/10.1016/0032-0633(95)00107-7)
- 737 Acton, C., Bachman, N., Semenov, B., & Wright, E. 2017,  
 738 Planetary and Space Science,  
 739 doi: [10.1016/j.pss.2017.02.013](https://doi.org/10.1016/j.pss.2017.02.013)
- 740 Azari, A., Biersteker, J., Ryan Dewey, G. D., Forsberg, E.,  
 741 & et al., C. H. 2020, doi: [10.48550/arXiv.2007.15129](https://arxiv.org/abs/2007.15129)
- 742 Barnes, J. W., Buratti, B. J., Turtle, E. P., et al. 2013,  
 743 Planetary Science, 2, 1, doi: [10.1186/2191-2521-2-1](https://doi.org/10.1186/2191-2521-2-1)
- 744 Barnes, J. W., Turtle, E. P., Trainer, M. G., et al. 2021,  
 745 The Planetary Science Journal, 2, 130,  
 746 doi: [10.3847/psj/abfdcf](https://doi.org/10.3847/psj/abfdcf)
- 747 Barth, E. L., & Rafkin, S. C. 2007, Geophysical Research  
 748 Letters, 34  
 749 —. 2010, Icarus, 206, 467
- 750 Brown, M., Roberts, J., & Schaller, E. 2010, Icarus, 205,  
 751 571, doi: [10.1016/j.icarus.2009.08.024](https://doi.org/10.1016/j.icarus.2009.08.024)
- 752 Burr, D. M., Drummond, S. A., Cartwright, R., Black,  
 753 B. A., & Perron, J. T. 2013a, Icarus, 226, 742,  
 754 doi: [10.1016/j.icarus.2013.06.016](https://doi.org/10.1016/j.icarus.2013.06.016)
- 755 Burr, D. M., Perron, J. T., Lamb, M. P., et al. 2013b, GSA  
 756 Bulletin, 125, 299
- 757 Caille, V., Maattanen, A., Spiga, A., & Falletti, L. 2022,  
 758 Journal of Geophysical Research: Planets, 128, 123,  
 759 doi: [10.1029/2022JE007384](https://doi.org/10.1029/2022JE007384)
- 760 Cao, X., Wipf, D., Wen, F., Duan, G., & Sun, J. 2013,  
 761 Proceedings of the IEEE International Conference on  
 762 Computer Vision (ICCV), 3208-3215,  
 763 doi: [10.1109/ICCV.2013.398](https://doi.org/10.1109/ICCV.2013.398).
- 764 Chanover, N., Bauer, J., Blalock, J., et al. 2022, Remote  
 765 Sensing, 13, 6112, doi: [10.3390/rs14236112](https://doi.org/10.3390/rs14236112)
- 766 Chen, Y., Weng, Q., Tang, L., Liu, Q., & Fan, R. 2021,  
 767 IEEE Geoscience and Remote Sensing Letters, 19,  
 768 doi: [10.1109/LGRS.2021.3102970](https://doi.org/10.1109/LGRS.2021.3102970)
- 769 Di, K., Li, W., Yue, Z., Sun, Y., & Liu, Y. 2014, Advances  
 770 in Space Research, 54, 2419,  
 771 doi: [10.1016/j.asr.2014.08.018](https://doi.org/10.1016/j.asr.2014.08.018)
- 772 Dundar, M., Ehlmann, B. L., & Leask, E. K. 2019, Earth  
 773 and Planetary Astrophysics,  
 774 doi: [10.48550/arXiv.1909.02387](https://doi.org/10.48550/arXiv.1909.02387)
- 775 et al., S. R. F. S. S. M. S. L. M. 2010, IEEE Workshop on  
 776 Hyperspectral Image and Signal Processing: Evolution in  
 777 Remote Sensing, 2, 1,  
 778 doi: [10.1109/WHISPERS.2010.5594893](https://doi.org/10.1109/WHISPERS.2010.5594893)
- 779 Francis, A., Sidiropoulos, P., & Muller, J.-P. 2019, Remote  
 780 Sensing, 11, 2312, doi: [10.3390/rs11192312](https://doi.org/10.3390/rs11192312)
- 781 Fulchignoni, M., Ferri, F., Angrilli, F., et al. 2005, Nature,  
 782 438, 785, doi: [10.1038/nature04314](https://doi.org/10.1038/nature04314)
- 783 Garvin, J. B., Getty, S. A., Arney, G. N., et al. 2022, The  
 784 Planetary Science Journal, 3, 17,  
 785 doi: [10.3847/PSJ/ac63c2](https://doi.org/10.3847/PSJ/ac63c2)

- 786 Goff, M. L., Tourneret, J.-Y., Wendt, H., Ortner, M., &  
 787 Spigai, M. 2017, ICPRS (8th International Conference of  
 788 Pattern Recognition Systems), 8, 197,  
 789 doi: [10.1049/cp.2017.0139ff.ffa1-01783857](https://doi.org/10.1049/cp.2017.0139ff.ffa1-01783857)
- 790 Gopalakrishnana, K., Khaitanb, S., Choudharya, A., &  
 791 Agrawal, A. 2017, Construction and Building Materials,  
 792 157, 322, doi: [10.1016/j.conbuildmat.2017.09.110](https://doi.org/10.1016/j.conbuildmat.2017.09.110)
- 793 Griffith, C. A., Hall, J. L., & Geballe, T. R. 2000, Science,  
 794 290, 509, doi: [10.1126/science.290.5491.509](https://doi.org/10.1126/science.290.5491.509)
- 795 Griffith, C. A., Owen, T., Miller, G. A., & Geballe, T. 1998,  
 796 Nature, 395, 575, doi: [10.1038/26920](https://doi.org/10.1038/26920)
- 797 Griffith, C. A., Penteado, P., Baines, K., et al. 2005,  
 798 Science, 310, 474, doi: [10.1126/science.1117702](https://doi.org/10.1126/science.1117702)
- 799 Griffith, C. A., Penteado, P., Rodriguez, S., et al. 2009,  
 800 Astrophysical Journal Letters, 702, L105,  
 801 doi: [10.1088/0004-637X/702/2/L105](https://doi.org/10.1088/0004-637X/702/2/L105)
- 802 He, K., Zhang, X., Ren, S., & Sun, J. 2015,  
 803 doi: <https://doi.org/10.48550/arXiv.1512.03385>
- 804 Kentsch, S., Caceres, M. L. L., Serrano, D., Roure, F., &  
 805 Diez, Y. 2020, Remote Sensing, 12, 1287,  
 806 doi: [10.3390/rs12081287](https://doi.org/10.3390/rs12081287)
- 807 Krizhevsky, A., Sutskever, I., & Hinton, G. 2012, Advances  
 808 in Neural Information Processing Systems, 25,  
 809 doi: [10.1145/3065386](https://doi.org/10.1145/3065386)
- 810 LeCun, Y., Bengio, Y., & Hinton, G. 2015, Nature, 521,  
 811 436, doi: [10.1038/nature14539](https://doi.org/10.1038/nature14539)
- 812 Letu, H., Nagao, T., Nakajima, T., & Matsumae, Y. 2022,  
 813 Applied Optics, 53, 7523, doi: [10.1364/AO.53.007523](https://doi.org/10.1364/AO.53.007523)
- 814 Li, L., Li, X., Jiang, L., Su, X., & Chen, F. 2021, Signal,  
 815 Video, and Image Processing, 15, 1527,  
 816 doi: [10.1007/s11760-021-01885-7](https://doi.org/10.1007/s11760-021-01885-7)
- 817 Li, X., Grandvalet, Y., Davoine, F., et al. 2020, Image and  
 818 Computing Vision, 93, doi: [10.1016/j.imavis.2019.103853](https://doi.org/10.1016/j.imavis.2019.103853)
- 819 Li, Z., Shen, H., Cheng, Q., et al. 2019, ISPRS Journal of  
 820 Photogrammetry and Remote Sensing, 150, 197,  
 821 doi: [10.1016/j.isprsjprs.2019.02.017](https://doi.org/10.1016/j.isprsjprs.2019.02.017)
- 822 Lin, T., Maire, M., Belongie, S. J., et al. 2014, CoRR,  
 823 abs/1405.0312. <https://arxiv.org/abs/1405.0312>
- 824 Lopez-Puigdollers, D., Mateo-Garcia, G., & Gomez-Chova,  
 825 L. 2021, Remote Sensing, 13, 992,  
 826 doi: [10.3390/rs13050992](https://doi.org/10.3390/rs13050992)
- 827 Lora, J. M., Lunine, J. I., & Russell, J. L. 2015, Icarus, 250,  
 828 516, doi: <https://doi.org/10.1016/j.icarus.2014.12.030>
- 829 Lorenz, R. D. 1993, Planetary and Space Science, 41, 647,  
 830 doi: [https://doi.org/10.1016/0032-0633\(93\)90048-7](https://doi.org/10.1016/0032-0633(93)90048-7)
- 831 Lorenz, R. D., Lopes, R. M., Paganelli, F., et al. 2008,  
 832 Planetary and Space Science, 56, 1132
- 833 Machado, P., Peralta, J., Silva, J., et al. 2022, Atmosphere,  
 834 13, 337, doi: [10.3390/atmos13020337](https://doi.org/10.3390/atmos13020337)
- 835 MacKenzie, S. M., Barnes, J. W., Sotin, C., et al. 2014,  
 836 Icarus, 243, 191, doi: [10.1016/j.icarus.2014.08.022](https://doi.org/10.1016/j.icarus.2014.08.022)
- 837 Mahajan, S., & Fataniya, B. 2020, Complex & Intelligent  
 838 Systems, 6, 251, doi: [10.1007/s40747-019-00128-0](https://doi.org/10.1007/s40747-019-00128-0)
- 839 Mitchell, J. L., Ádámkovics, M., Caballero, R., & Turtle,  
 840 E. P. 2011, Nature Geoscience, 4, 589,  
 841 doi: [10.1038/ngeo1219](https://doi.org/10.1038/ngeo1219)
- 842 Mommer, M. 2020, The American Astronomical Society,  
 843 doi: [10.3847/1538-3881/ab744f](https://doi.org/10.3847/1538-3881/ab744f)
- 844 Mouelic, S. L., Rodriguez, S., Robidel, R., et al. 2018,  
 845 Icarus, 311, 371,  
 846 doi: <https://doi.org/10.1016/j.icarus.2018.04.028>
- 847 Phillips, C. B., & Pappalardo, R. T. 2014, Eos,  
 848 Transactions American Geophysical Union, 95, 165,  
 849 doi: [10.1002/2014EO200002](https://doi.org/10.1002/2014EO200002)
- 850 Porco, C., West, R., Squyres, S., et al. 2004, Space Science  
 851 Reviews, 115, 363, doi: [10.1007/s11214-004-1456-7](https://doi.org/10.1007/s11214-004-1456-7)
- 852 Rafkin, S. C., & Barth, E. 2015, Journal of Geophysical  
 853 Research: Planets, 120, 739
- 854 Rafkin, S. C., Lora, J. M., Soto, A., & Battalio, J. M. 2022,  
 855 Icarus, 373, 114755
- 856 Rafkin, S. C., & Soto, A. 2020, Icarus, 351, 113903
- 857 Rodriguez, S., Mouelic, S., Rannou, P., Tobie, G., & et al.,  
 858 K. B. 2009, Nature, 459, 678, doi: [10.1038/nature08014](https://doi.org/10.1038/nature08014)
- 859 Rodriguez, S., Mouelic, S. L., Rannou, P., et al. 2011,  
 860 Icarus, 216, 89,  
 861 doi: <https://doi.org/10.1016/j.icarus.2011.07.031>
- 862 Schaller, E. L., Brown, M. E., Roe, H. G., & Bouchez, A. H.  
 863 2006a, Icarus, 182, 224, doi: [10.1016/j.icarus.2005.12.021](https://doi.org/10.1016/j.icarus.2005.12.021)
- 864 Schaller, E. L., Brown, M. E., Roe, H. G., Bouchez, A. H.,  
 865 & Trujillo, C. A. 2006b, Icarus, 184, 517,  
 866 doi: [10.1016/j.icarus.2006.05.025](https://doi.org/10.1016/j.icarus.2006.05.025)
- 867 Seignovert, B., Rannou, P., West, R. A., & Vinatier, S.  
 868 2021, The Astrophysical Journal, 907, 17,  
 869 doi: <https://doi.org/10.3847/1538-4357/abcd3b>
- 870 Seignovert, B., Rannou, P., Lavvas, P., Cours, T., & West,  
 871 R. A. 2017, Icarus, 292, 13,  
 872 doi: [http://doi.org/10.1016/j.icarus.2017.03.026](https://doi.org/10.1016/j.icarus.2017.03.026)
- 873 Simonyan, K., & Zisserman, A. 2015, arXiv, 1409.1556
- 874 Stofan, E. R., Lunine, J. I., Lopes, R., et al. 2006, Icarus,  
 875 185, 443, doi: [10.1016/j.icarus.2006.07.015](https://doi.org/10.1016/j.icarus.2006.07.015)
- 876 Tomasko, M. G., Archinal, B., Becker, T., et al. 2005,  
 877 Nature, 438, 765, doi: [10.1038/nature04126](https://doi.org/10.1038/nature04126)
- 878 Turtle, E., Delgenio, A., John, B., Perry, J., & et al., E. S.  
 879 2011, Geophysical Research Letters, 38, 571,  
 880 doi: [10.1029/2010GL046266](https://doi.org/10.1029/2010GL046266)
- 881 Turtle, E., Perry, J. E., Barbara, J. M., Genio, A. D. D., &  
 882 et al., S. R. 2018, Geophysical Research Letters, 45, 5320,  
 883 doi: [10.1029/2018GL078170](https://doi.org/10.1029/2018GL078170)

- 884 Turtle, E. P., Perry, J. E., Hayes, A. G., et al. 2011,  
885 Science, 331, 1414, doi: [10.1126/science.1201063](https://doi.org/10.1126/science.1201063)
- 886 Wilkins, A., Cocke, S., McDaniel, J., Santerre, J., & Nixon,  
887 C. 2020, SMU Data Science Review, 3
- 888 Zhang, Y., Li, W., Tao, R., et al. 2021a, IEEE Transactions  
889 on Geosciences and Remote Sensing, 19, 9646,  
890 doi: [10.1109/TGRS.2020.3046756](https://doi.org/10.1109/TGRS.2020.3046756)
- 891 Zhang, Y., Li, W., Zhang, M., et al. 2021b, IEEE Trans  
892 Neural Netw Learn Syst,  
893 doi: [10.1109/TNNLS.2021.3109872](https://doi.org/10.1109/TNNLS.2021.3109872)
- 894 —. 2022, IEEE Trans Neural Netw Learn Syst,  
895 doi: [10.1109/TNNLS.2022.3185795](https://doi.org/10.1109/TNNLS.2022.3185795)
- 896 Zhuang, F., Qi, Z., Duan, K., Xi, D., & Yongchun Zhu,  
897 H. Z. 2020, Proceedings of the IEEE, 109, 43,  
898 doi: [10.1109/JPROC.2020.3004555](https://doi.org/10.1109/JPROC.2020.3004555)